



Parent–Child Well Spacing Optimization in Deep Shale Gas Reservoir with Two Complex Natural Fracture Patterns: A Sichuan Basin Case Study

Yanli Pei¹ · Jianfa Wu² · Cheng Chang² · Chuxi Liu¹ · Kan Wu³ · Wei Yu⁴ · Jijun Miao⁴ · Zhenyu Mao⁵ · Kamy Sepehrnoori¹

Received: 21 January 2022 / Accepted: 23 June 2022 / Published online: 20 July 2022
© The Author(s), under exclusive licence to Springer Nature B.V. 2022

Abstract

An integrated reservoir-geomechanics-fracture model is implemented in a deep shale gas reservoir in the Sichuan Basin, Western China, to optimize the parent–child well spacing under various complex natural fracture settings. The integrated multiphysics model employs an embedded discrete fracture model to characterize fluid flow through complex natural and hydraulic fractures, a finite element method geomechanics model to predict the 3D spatiotemporal stress changes, and a displacement discontinuity method hydraulic fracture model to simulate the multicluster fracture propagation under the depletion-induced heterogeneous stress field. Field case studies on two complex natural fracture patterns (i.e., orthogonal and clustered natural fractures) show that (a) the orientation change of maximum horizontal stress (S_{Hmax}) is negligible since the target shale gas reservoir is highly stressed and under large horizontal stress contrast; (b) the decrease in minimum horizontal stress (S_{Hmin}) over the stimulated reservoir volume is about 30–50% of pore pressure drop due to the rapid pressure depletion; (c) decreasing the parent–child horizontal/vertical spacing or elongating the production time aggravates the asymmetry growth of child-well fractures in either natural fracture pattern; (d) the parent and child wells are suggested to space farther under the clustered natural fracture pattern to avoid undesirable interwell fracture interference caused by the irregular localized stress sink. This work delivers a comprehensive understanding of the geomechanics consequences under different natural fracture settings and provides practical guidance on infill operations in layered formations of the Sichuan Basin.

✉ Yanli Pei
yanli.pei@utexas.edu

¹ Hildebrand Department of Petroleum and Geosystems Engineering, The University of Texas at Austin, Austin, TX 78712, USA

² Petrochina Southwest Oil & Gas Field Company, Chengdu, China

³ Harold Vance Department of Petroleum Engineering, Texas A&M University, College Station, TX 77843, USA

⁴ SimTech LLC, Katy, TX 77494, USA

⁵ Beijing Karst Science & Technology LTD, Beijing, China

Article Highlights

- An integrated reservoir-geomechanics-fracture model is employed to optimize the parent–child well spacing in a multilayer deep shale gas reservoir with complex natural fractures
- The complex fracture network, in situ stress change, and multicluster fracture propagation are simulated by EDFM, FEM geomechanics model, and DDM hydraulic fracture model, respectively
- The impacts of orthogonal and clustered natural fractures on spatiotemporal stress evolution and parent–child well layout are investigated based on actual field datasets
- The parent–child well spacing is optimized by incorporating geomechanics responses in addition to fluid-flow simulation to provide hands-on guidance for the Sichuan Basin

Keywords Geomechanics · Parent–child well spacing · Deep shale gas reservoir · Complex natural fractures · Sichuan Basin

Nomenclatures

a	One-half element length (m)
a_{\max}	Langmuir volume ($\text{m}^3 \text{kg}^{-1}$)
A	Area (m^2)
\mathbf{b}	Body force (m s^{-2})
d	Average distance (m)
D	Displacement of elements (m)
\mathbf{D}	Stiffness tensor (MPa)
E	Young's modulus (GPa)
K	Stress intensity factor ($\text{MPa m}^{0.5}$)
\mathbf{K}	Permeability tensor (mD)
L	Length of fracture-intersection line (m)
\mathbf{n}_f	Normal vector of the fracture plane, dimensionless
p	Pore pressure (MPa)
P_c	Langmuir pressure (MPa)
q	Sink or source rate ($\text{kg m}^{-3} \text{s}^{-1}$)
q_{ads}	Adsorption term, dimensionless
S	Saturation (%)
S_0	Cohesion (MPa)
T	Transmissibility factor (mD-m)
\mathbf{u}	Displacement vector (m)
\mathbf{v}	Darcy's velocity (m s^{-1})
w	Fracture aperture (m)
α	Biot–Willis coefficient, dimensionless
γ	Permeability decay coefficient (MPa^{-1})
δ	Kronecker delta, dimensionless
$\boldsymbol{\varepsilon}$	Strain tensor, dimensionless
μ	Friction coefficient, dimensionless
ν	Poisson's ratio, dimensionless
ρ	Density (kg m^{-3})

σ	Total stress tensor (MPa)
$\sigma_{n\beta}$	Normal stress on the interface (MPa)
τ_{β}	Shear stress on the interface (MPa)
ϕ	Porosity (%)

1 Introduction

Despite some developers still relying on empirical knowledge or pressure responses for layered unconventional reservoir management (Lindsay et al. 2018; Behm et al. 2019; Chen et al. 2021), there is growing consent on the importance of geomechanics impacts in the industry. For example, the depletion-induced stress sink (i.e., significant stress drop) or stress vortex (i.e., convergence of maximum stress azimuth) over the stimulated reservoir volume (SRV) has been found to trigger interference between parent and child wells and damage the well performance (Marongiu-Porcu et al. 2016; Safari et al. 2017). Meanwhile, three-dimensional complex natural fractures are widely observed in tight shale formations—field practice in the Sichuan Basin reports different natural fracture patterns (Liang et al. 2015; Jun et al. 2017; Liu et al. 2019; Pei et al. 2020), which further aggravates the complexity of flow and geomechanics interactions in layered formations. Hence, comprehending the 3D spatiotemporal stress changes under complex natural fracture settings is critical to guaranteeing the effective development of stacked unconventional reservoirs.

At the early stage of unconventional development, drilling production wells to the same potential pay zone was the industry trend, so many studies in the literature investigated the local stress evolution in single-layer formation. Roussel et al. (2013) modeled the occurrence of stress reorientation between two fractured horizontal wells in a liquid-rich shale reservoir, upon which they demonstrated how the disturbed stress state would curve the newly induced fractures to orient parallel to the child well (i.e., infill well). Based on an Eagle Ford Shale case, Marongiu-Porcu et al. (2016) further investigated the underlying mechanisms of fracture deflection and fracture hits from the perspective of depletion-induced stress changes. They indicated that optimizing the infill timing and well placement is a feasible way to avoid significant interwell fracturing interference. Guo et al. (2018) and Sangnimnuan et al. (2018) extended the scope of geomechanics study in the 2D environment by incorporating more complex fracture geometries, such as nonuniform, nonplanar, and slanted hydraulic fractures, into their coupled hydromechanical modeling. Taking the geomechanics effects into unconventional development resolves some thorny problems on-site; however, the studies mentioned above are still limited to the horizontal propagation of stress changes.

Recently, the prevalence of three-dimensional multilayer exploitation has boosted research on the vertical propagation of stress alteration. Preliminary studies indicate that the parent-well production not only changes the orientation and magnitude of local principal stresses in the producing layer but alters the in situ stress state in adjacent potential layers (Sangnimnuan et al. 2019; Pei and Sepehrnoori 2022). In detail, Ajisafe et al. (2017) simulated the production-induced spatiotemporal stress evolution in a layered shale reservoir of the Delaware Basin and captured the cross-layer stress interference that impairs the infill well fracturing. Defeu et al. (2019) also quantified the impacts of interlayer stress interference on the landing depth of child wells within a depleted stacked reservoir in the Midland Basin. To provide an integral solution of infill-well design in multilayer reservoirs, Pei et al. (2021) proposed a multiphysics, integrated reservoir-geomechanics-fracture

model and applied it to the Bone Spring Formation in the Permian Basin to optimize the development strategy (e.g., timing and locations) of the upside target. Although these studies have further incorporated 3D geomechanics analyses, most focus on stress changes introduced by hydraulic fractures. There still lacks a comprehensive study that fully addresses the infill-well placement challenge when complex natural fractures exist.

Since complex natural fractures widely exist in our target deep shale gas reservoir of the Sichuan Basin, we extend our integrated reservoir-geomechanics-fracture model (Pei et al. 2021) to more complex geologic and fracture settings, simulate the 3D spatiotemporal stress evolution under complex natural fractures, and uncover the associated impacts on the child-well placement in layered formations. For either orthogonal or clustered natural fracture pattern, the poroelastic response between fluid flow and rock matrix is modeled with the aid of embedded discrete fracture model (EDFM) and finite element method (FEM), and the multicluster child-well fracture propagation is simulated with the displacement discontinuity method (DDM) hydraulic fracture model under the production-disturbed heterogeneous stress state. In field case studies, we consider two possible infill layouts (e.g., infill well in the producing layer or the upper potential layers) and optimize the horizontal and vertical spacing between parent and child wells accordingly. The outcomes of this study bring new insights into the stress evolution under complex natural fractures and provide hands-on guidelines for infill operations in the deep shale gas reservoir of the Sichuan Basin.

2 Methodology

2.1 Coupled Flow and Geomechanics Model

In the gas/water two-phase system, the mass conservation equation for each phase l in the matrix domain (m) and fracture domain (f), respectively, is

$$\frac{\partial}{\partial t} (\phi_m S_{l,m} \rho_l + \rho_l q_{\text{ads}}) + \nabla \cdot (\rho_l \mathbf{v}_{l,m}) = q_{l,m} - q_{l,mf}, \quad (1)$$

$$\frac{\partial}{\partial t} (\phi_f S_{l,f} \rho_l) + \nabla \cdot (\rho_l \mathbf{v}_{l,f}) = q_{l,f} + q_{l,mf}, \quad (2)$$

where ϕ_m , ϕ_f are porosity for the matrix and fracture domains, $S_{l,m}$, $S_{l,f}$ are the phase saturation in the matrix and fracture domains, ρ_l is the fluid density, q_{ads} is the adsorption term, $\mathbf{v}_{l,m}$, $\mathbf{v}_{l,f}$ are Darcy's velocity in the matrix and fracture domains, $q_{l,m}$, $q_{l,f}$ are the source/sink term in the matrix and fracture domains, and $q_{l,mf}$ is the mass flux between matrix and fracture.

The fluid flow in a tight shale formation is affected by a series of underlying physics, such as gas desorption, Knudsen diffusion, and capillary blocking (Liu et al. 2020; Wang et al. 2021), among which the gas desorption is suggested as one of the major contributing factors to shale gas production (Yu and Sepehrnoori 2014; Mi et al. 2018). Hence, this work ignores the effects of Knudsen diffusion and gas slippage on the apparent permeability but incorporates the shale gas desorption effect in the fluid-flow simulation. The adsorption term is calculated by the Langmuir isotherm (Langmuir 1918) as

$$q_{\text{ads}} = \delta_l B_l (1 - \phi) \rho_s a_{\text{max}} \frac{b P_c}{1 + b P_c}, \quad (3)$$

where δ_l is the phase indicator ($\delta_l = 1$ for gas and 0 for water), B_l is the formation volume factor, ρ_s is the bulk density, a_{max} is the Langmuir volume, b is the inverse of average pore pressure, and P_c is the Langmuir pressure.

The complex mass flux between matrix and fracture cells or fracture and fracture cells is characterized by a generalized form of EDFM (Li and Lee 2008; Moïfar et al. 2014; Xu et al. 2019). Under the framework of EDFM, we discretize fractures into small control volumes upon matrix-gridblock boundaries, introduce additional fracture cells to the structured gridding of the matrix, and link non-neighboring cells with the definition of non-neighboring connections (NNCs). The NNCs transmissibility for fluid flow between matrix and fracture segment, T_{m-f} , and between fracture segments in an individual fracture or of intersecting fractures, T_{f-f} , can be written as

$$T_{m-f} = \frac{2A_f (\mathbf{K} \cdot \mathbf{n}_f) \cdot \mathbf{n}_f}{d_{m-f}}, \quad (4)$$

$$T_{f-f} = \frac{T_{f1} T_{f2}}{T_{f1} + T_{f2}}, T_{f1} = \frac{k_{f1} w_{f1} L_{\text{int}}}{d_{f1}}, T_{f2} = \frac{k_{f2} w_{f2} L_{\text{int}}}{d_{f2}}, \quad (5)$$

where A_f is the area of the fracture segment on one side, \mathbf{K} is the permeability tensor of the matrix gridblock, \mathbf{n}_f is the normal vector of the fracture plane, k_f is the permeability of fracture segment, w_f is the aperture of fracture segment, L_{int} is the intersection length of two fracture segments, and d is the weighted average of the normal distance from the centroids of fracture segments to the intersection line. More detailed demonstrations of the NNCs transmissibility can be found in Sepehrnoori et al. (2020).

In a highly fractured system, the deformation of fractures typically dominates because of the weaker mechanical strength at fracture surfaces (Liu 2017; Wang and Fidelibus 2021). Hence, this work ignores the matrix permeability change but addresses the fracture conductivity variation with pressure drawdown. To be noted, the fracture permeability decrease associated with reservoir depletion is modeled through the compaction/dilation option in an exponential form (Settari et al. 2005; Bachman et al. 2011)

$$k_f = k_{f0} e^{-\gamma(p_0 - p)}, \quad (6)$$

where k_f is the fracture permeability at average pore pressure p , k_{f0} is the initial fracture permeability at the reference pressure p_0 , and γ is the fracture permeability decay coefficient.

The governing equation of the geomechanics model is derived from the linear momentum balance as

$$\nabla \cdot \boldsymbol{\sigma} + \rho \mathbf{b} = 0, \quad (7)$$

where $\boldsymbol{\sigma}$ denotes the total stress tensor, ρ is the total mass density, and \mathbf{b} is the body force.

The rock deformation can be approximated via a linear isotropic poroelastic model (Biot 1941, 1955), which is

$$\boldsymbol{\sigma} - \boldsymbol{\sigma}_0 = \mathbf{D} : \boldsymbol{\varepsilon} - \alpha(p - p_0) \boldsymbol{\delta}, \quad (8)$$

where \mathbf{D} is the stiffness tensor, $\boldsymbol{\varepsilon}$ is the strain tensor, α is the Biot–Willis coefficient, p is the average pore pressure calculated from the fluid-flow model, $\boldsymbol{\delta}$ is the Kronecker delta, and $\boldsymbol{\sigma}_0$ and p_0 are the total stress tensor and average pore pressure at the reference state, respectively.

Based on the small strain theory, the strain tensor is written in terms of the displacement as

$$\boldsymbol{\varepsilon} = \frac{1}{2}(\nabla \mathbf{u} + \nabla^T \mathbf{u}), \tag{9}$$

where \mathbf{u} is the displacement vector.

The unknowns in the geomechanics model, i.e., nodal displacement and elemental strain/stress, are solved using FEM with linear hexahedron elements. The orientation of horizontal principal stresses (i.e., S_{Hmax} or S_{Hmin}) can be rotated clockwise or counterclockwise (Fig. 1) due to the depletion anisotropy at a localized gridblock, and the magnitude of horizontal principal stresses also changes in the production process. More details on how to calculate the updated in situ stress state can be found in Pei et al. (2021).

2.2 Complex Hydraulic Fracture Model

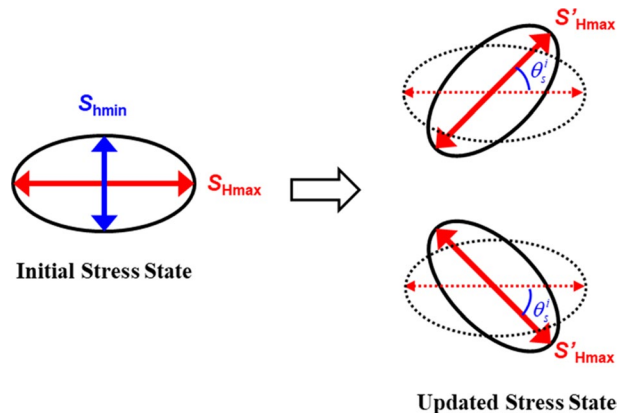
Under the depletion-induced heterogeneous stress state, the simplified 3D DDM model is applied to simulate the complex hydraulic fracture propagation. The normal and shear displacement discontinuities at element j , D_n^j and D_s^j , are solved using a system of equations (Wu and Olson 2015; Li et al. 2018; Wang et al. 2020) as

$$\sigma_n^i = \sum_{j=1}^N G^{ij} C_{nn}^{ij} D_n^j + \sum_{j=1}^N G^{ij} C_{ns}^{ij} D_s^j, \tag{10}$$

$$\sigma_s^i = \sum_{j=1}^N G^{ij} C_{sn}^{ij} D_n^j + \sum_{j=1}^N G^{ij} C_{ss}^{ij} D_s^j, \tag{11}$$

where σ_n^i and σ_s^i are the normal and shear stresses imposed on the boundary element i , which can be approximated from the above coupled flow and geomechanics model, G^{ij} is a 3D correction factor, C_{nn}^{ij} is the normal stress at element i induced by a normal

Fig. 1 Illustration of stress reorientation on a plane normal to the vertical principal stress



displacement discontinuity at element j , and C_{ns}^{ij} is the normal stress at element i caused by a shear displacement discontinuity at element j . The illustration of C_{sn}^{ij} and C_{ss}^{ij} follows a similar approach to that of C_{nm}^{ij} and C_{ns}^{ij} .

The fracture propagation direction is calculated based on the maximum circumferential stress criterion, in which the opening and shearing stress intensity factors, K_I and K_{II} , are determined from the normal and shear displacement discontinuities, D_n and D_s , at the fracture tip element (Olson 2007) as

$$K_I = \frac{0.806E\sqrt{\pi}}{4(1-\nu^2)\sqrt{2a}}D_n, \tag{12}$$

$$K_{II} = \frac{0.806E\sqrt{\pi}}{4(1-\nu^2)\sqrt{2a}}D_s, \tag{13}$$

where E is Young’s modulus, ν is the Poisson’s ratio, and a is the one-half element length.

The interaction between natural and hydraulic fractures is modeled using the Mohr–Coulomb failure criterion (Wu and Olson 2016). When a hydraulic fracture approaches a frictional interface (Fig. 2), the hydraulic fracture will be arrested and diverted into the natural fracture if

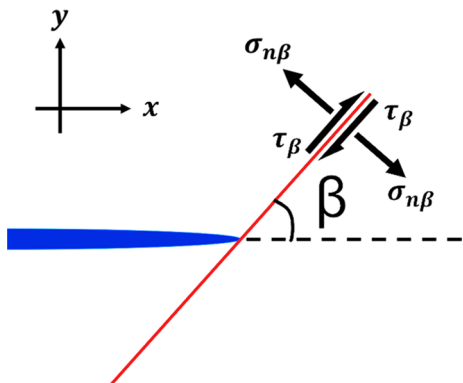
$$|\tau_\beta| \geq S_o + \mu\sigma_{n\beta}, \tag{14}$$

where μ is the friction coefficient, S_o is the cohesion of the interface, τ_β and $\sigma_{n\beta}$ are the shear and normal stresses acting on the interface, and β is the natural-hydraulic fracture contacting angle. Otherwise, the hydraulic fracture will cross the natural fracture if the maximum tensile stress on the other side of the interface reaches the tensile strength of the rock.

2.3 Integrated Reservoir-Geomechanics-Fracture Model

The integrated reservoir-geomechanics-fracture model proposed in Pei et al. (2021) is enhanced and adapted in this work to optimize the parent–child well spacing under complex natural fracture settings. As shown in Fig. 3, the integrated reservoir-geomechanics-fracture

Fig. 2 Schematic of a hydraulic fracture approaching a natural fracture interface



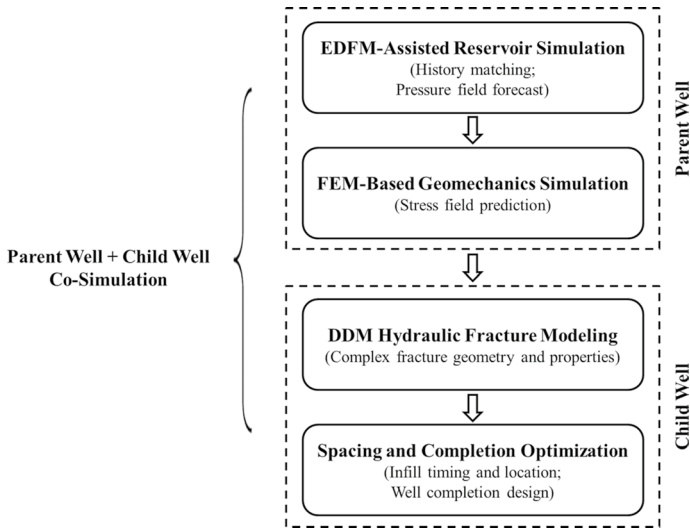


Fig. 3 Diagram of the integrated reservoir-geomechanics-fracture model

model includes three closely connected parts—parent-well simulation, child-well simulation, and parent–child well co-simulation. For the parent-well section, the field-measured pressure and flow rates are first matched by tuning reservoir and fracture properties. Next, pore pressure changes are forecast with EDFM characterizing complex natural and hydraulic fractures. The updated pore pressure is then passed to the FEM-based geomechanics model to predict the 3D spatiotemporal stress evolution. Note that the variation of fracture permeability associated with stress changes is incorporated into the reservoir model through the compaction/dilation option. Once the new pressure and stress state are attained, the integrated model moves to the child-well section. The DDM hydraulic fracture model is employed to simulate the child-well fracture propagation under a depletion-induced heterogeneous stress field. Based on the resultant fracturing effectiveness or well performance, the optimal timing, location, and completion of infill operations can be determined accordingly. Finally, as the third section of the integrated model, co-simulation of the parent-well and child-well production can be followed to evaluate the ultimate hydrocarbon recovery. To be noted, this work omits the simulation of well-pad performance and instead optimizes the parent–child well spacing based on the child-well fracturing effectiveness. The asymmetric growth of child-well fracture length and height is analyzed under various horizontal and vertical parent–child offset combinations, and the optimal parent–child well spacing is determined for in-layer and stacked infill layouts to avoid significant parent–child fracture interference. Please refer to Pei et al. (2021) for more detailed descriptions of the multiphysics integrated model.

3 Field Case Studies

This work focuses on a deep shale gas reservoir in the Sichuan Basin, Western China. Our geological model includes five pay zones of the Wufeng–Longmaxi shale, as listed in Table 1. Several horizontal wells have been drilled to produce the lower target (Wufeng

Table 1 Summary of the data used in the geological model

Formation	Thickness (m)	Porosity (%)	Adsorption gas (m ³ /t)	Gas saturation (%)	Abundance (10 ⁸ m ³ /km ²)
Longmaxi 1 ⁴	60.0	5.28	1.73	66.80	2.36
Longmaxi 1 ³	6.0	5.99	3.71	74.16	1.58
Longmaxi 1 ²	5.0	6.02	4.67	86.62	1.57
Longmaxi 1 ¹	1.5	5.53	4.66	83.27	0.48
Wufeng	10.0	4.38	2.44	72.63	0.91

and Longmaxi 1^{1–3}) since 2019, and the thick upper target (Longmaxi 1⁴) is also gas abundant but has not been exploited yet. Meanwhile, microseismic, imaging, and core data indicate that natural fractures are well developed in this area due to the complex tectonic environment and can be roughly categorized into two types: orthogonal and clustered natural fractures (Fig. 4). Field operations also find that orthogonal natural fractures are more conducive to the propagation of hydraulic fractures, thus creating longer ones. The clustered natural fractures, however, would hinder the extension of hydraulic fractures, especially when they are parallel to the parent wellbore. Thus, a more intensive completion design (i.e., higher proppant amount and smaller perforation cluster spacing) is generally applied on-site to enhance the hydraulic fracturing efficiency close to such clustered natural fractures. To better understand the impacts of complex natural fractures on the four-dimensional well layout, we select two representative wells, i.e., H1-2 and H10-4, to investigate the depletion-induced stress changes and optimize the parent–child well spacing based on child-well fracturing results. To be noted, Well H1-2 is surrounded by orthogonal natural fractures, and Well H10-4 by parallel, clustered natural fractures.

3.1 Type I: Orthogonal Natural Fracture Pattern

A real 3D geological model of Well H1-2 is built with detailed stratigraphic, petrophysical, and geomechanical information. Around Well H1-2, the orthogonal natural fracture pattern is identified, with a total of 1139 natural fractures widely distributed.

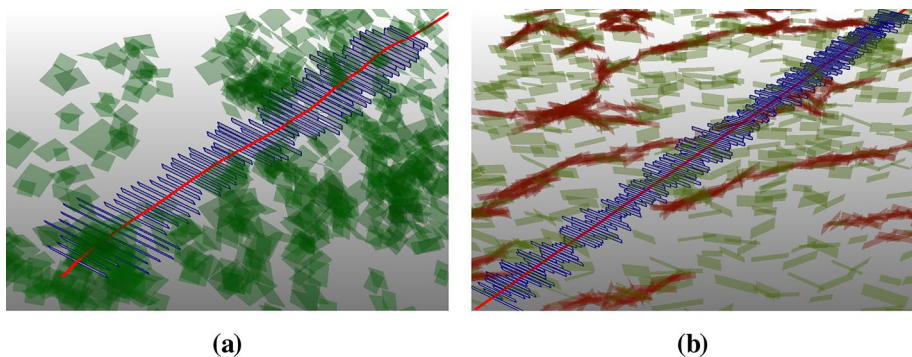


Fig. 4 Comparison of **a** orthogonal natural fractures and **b** clustered natural fractures. The red lines are the horizontal wellbore, and the blue surfaces are hydraulic fractures. The green and rusty red surfaces represent orthogonal and clustered natural fractures, respectively

To proceed with reservoir simulation, we upscale the fine-grid geological model into 10 sublayers following its geological structures. Each of Wufeng and Longmaxi 1^1 – 1^3 is gridded as 1 cell in the z -direction, and Longmaxi 1^4 is discretized to 6 cells vertically. The resultant corner-point reservoir model has a dimension of $960 \times 2160 \times 83$ m, and the gridblock size in the horizontal direction is approximately 15 m. Well H1-2 is drilled toward the lower production target and mainly completed in Longmaxi 1^1 and 1^2 at an average reservoir depth of 3358 m. Its horizontal lateral length of 1478 m is fractured in 23 stages with 3 clusters per stage and perforation cluster spacing of 14.25 m. Upon this basic information, we first calibrate the reservoir and fracture properties from history matching, then model the 3D spatiotemporal stress changes and optimize the parent–child well spacing with the aid of the hydraulic fracture model.

3.1.1 History Matching

For Well H1-2, there are 333 days of production data available for model calibration. The gas rates serve as the matching constraint, as shown in Fig. 5a. Two groups of uncertainty parameters, i.e., reservoir properties including matrix permeability, matrix water saturation, and relative permeability curves and hydraulic/natural fracture properties including fracture height, fracture half-length, fracture conductivity, fracture permeability decay coefficient, and fracture water saturation, are calibrated to match the history records of bottomhole pressure (BHP) and water rate. The stress dependency of discrete fractures is considered, and the history-matched fracture permeability decay coefficient is 0.02 MPa^{-1} .

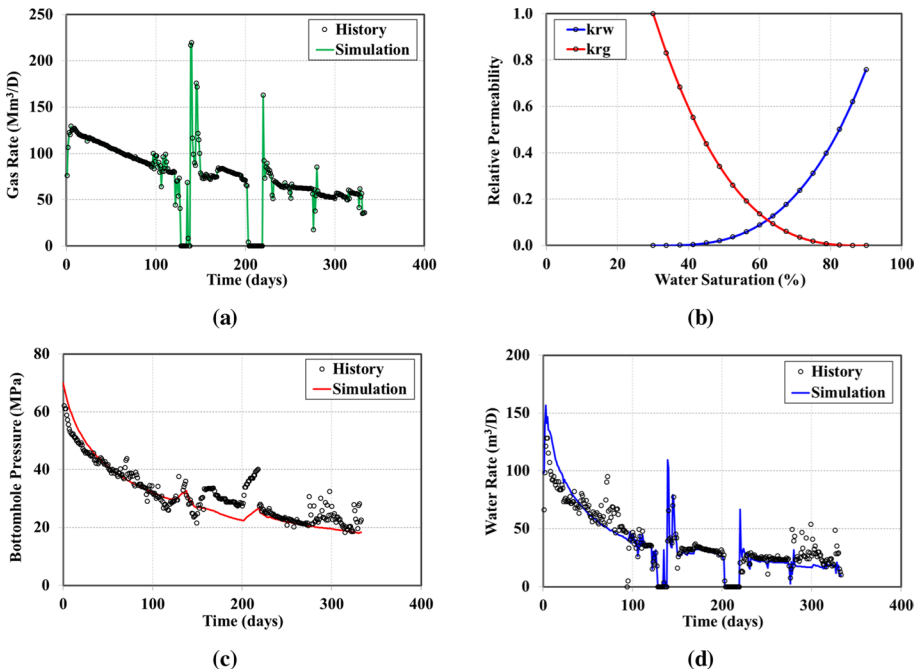
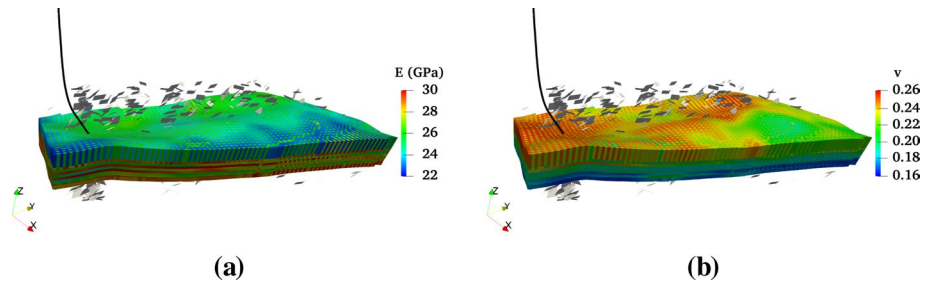


Fig. 5 History matching results for Well H1-2 with **a** gas rates as matching constraint, **b** history-matched relative permeability curves, **c** historical and simulated BHPs, and **d** historical and simulated water rates

Table 2 Calibrated reservoir and fracture parameters of Well H1-2

Reservoir properties	Value	Unit	Fracture properties	Value	Unit
Initial reservoir pressure	70	MPa	Horizontal lateral length	1478	m
Reservoir temperature	150	°C	Number of stages	23	–
Average reservoir porosity	5.7	%	Number of clusters	69	–
Horizontal permeability	185	nD	Perforation cluster spacing	14.25	m
Vertical permeability	1.9	nD	Average fracture half-length	73	m
Rock compressibility	4.35×10^{-4}	MPa^{-1}	Average fracture height	6.82	m
Matrix water saturation	30	%	Hydraulic fracture conductivity	130	mD-m
Irreducible gas saturation	10	%	Natural fracture conductivity	11	mD-m
Langmuir volume	0.004	m^3/kg	Fracture perm decay coeff	0.02	MPa^{-1}
Langmuir pressure	10.3	MPa	Fracture water saturation	74.4	%
Bulk density	2600	kg/m^3	Number of natural fractures	1139	–

**Fig. 6** Heterogeneous distribution of **a** Young's modulus and **b** Poisson's ratio. The gray surfaces represent natural fractures, and the black line represents the trajectory of the horizontal wellbore

The relative permeability curves obtained from history matching are shown in Fig. 5b. Meanwhile, Fig. 5c, d shows a good match between simulated and history BHPs and water rates, respectively. The calibrated reservoir and fracture parameters of Well H1-2 are listed in Table 2.

3.1.2 Spatiotemporal Stress Evolution

Based on field and laboratory tests, the magnitude of S_{hmin} over which orthogonal natural fractures are distributed is about 90 MPa, and the horizontal stress contrast ($S_{Hmax} - S_{hmin}$) is 12 MPa. The heterogeneous Young's modulus and Poisson's ratio are included in the 3D geomechanics model, as shown in Fig. 6. Analysis of the spatiotemporal stress evolution consists of two aspects: (1) the orientation change of S_{Hmax} as it controls the propagation direction of hydraulic fractures; (2) the magnitude change of S_{hmin} as it determines the occurrence of stress sink and cross-well fracture interference. Hence, in this section, we model the orientation and magnitude change of local principal stresses in the 10 years of Well H1-2 production.

The pore pressure and S_{hmin} evolution with production time are presented in Fig. 7. As the pore pressure distribution indicates, Fig. 7a, b, the gas drainage volume grows both horizontally and vertically in time. The magnitude of S_{hmin} also drops significantly over the

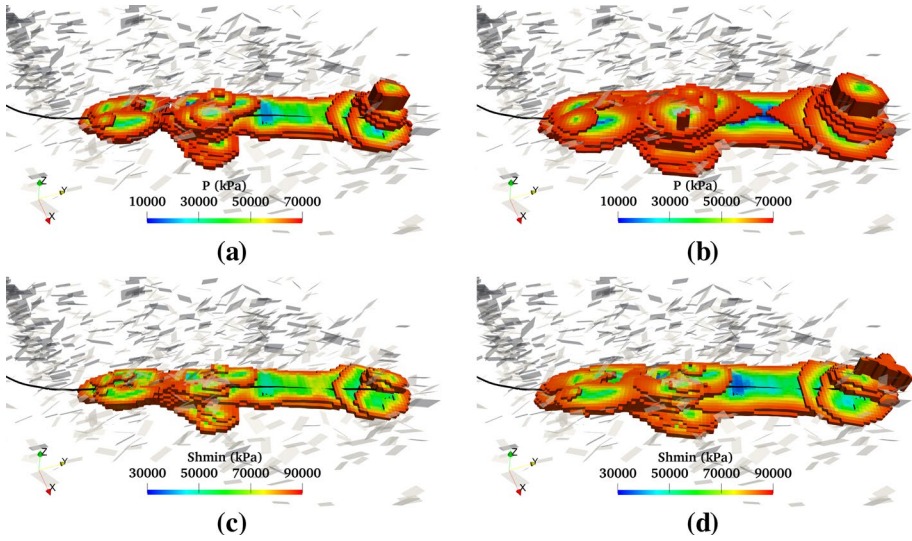


Fig. 7 Comparison of pore pressure and S_{hmin} changes around Well H1-2 with **a** pore pressure distribution at 2 years, **b** pore pressure distribution at 5 years, **c** S_{hmin} distribution at 2 years, and **d** S_{hmin} distribution at 5 years

drainage volume, as shown in Fig. 7c, d, and the changes in pore pressure and S_{hmin} magnitude tend to be positively correlated. Therefore, the rapid pore pressure depletion in deep shale gas reservoirs could be a dominant factor causing local principal stress to decrease in both producing and potential pay zones. On the other hand, Fig. 7 shows that the variation of S_{hmin} over time is much smaller than that of the pore pressure. A quantitative analysis of the pore pressure and S_{hmin} distribution within the SRV region is shown in Fig. 8. It can be seen that the histogram distribution for both pore pressure and S_{hmin} shifts leftwards as production time elongates; so does the empirical cumulative distribution function (ECDF). A comparison of ECDF P50 between pore pressure and S_{hmin} indicates that the decrease in S_{hmin} is about 50% of pore pressure drop at 2 years of parent-well production and 41% at 5 years.

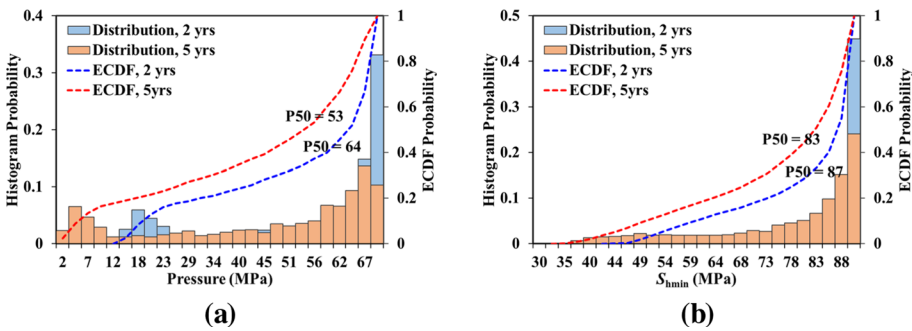


Fig. 8 Comparison of the histogram and ECDF probability between **a** pore pressure and **b** S_{hmin} over the SRV region at 2 and 5 years of Well H1-2 production

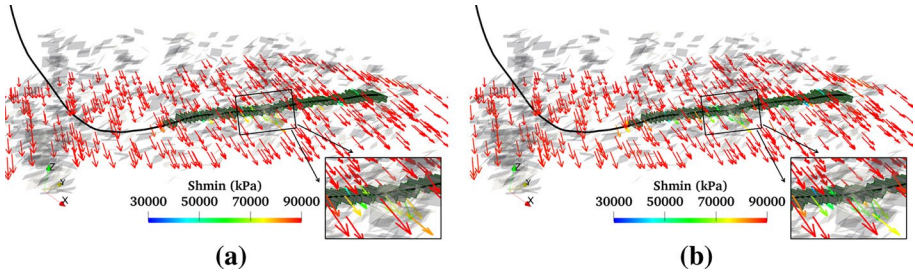


Fig. 9 Comparison of the orientation of S_{Hmax} (arrow directions) and magnitude of S_{hmin} (arrow colors) at **a** 2 years and **b** 5 years of Well H1-2 production

The arrow direction in Fig. 9 represents the orientation of S_{Hmax} . After 2 or 5 years, most regions still preserve the initial orientation of S_{Hmax} that is perpendicular to the horizontal wellbore. Though significant S_{hmin} drop is observed around the wellbore, as indicated by light arrow colors, no obvious stress rotation occurs due to the relatively high horizontal stress contrast (12 MPa) over the target area. In other words, the drainage rate difference in parallel and perpendicular directions to the horizontal well is not strong enough to overcome the in situ horizontal stress contrast. To further quantify the orientation change of S_{Hmax} , we define impact radius as the maximum distance from the horizontal wellbore to where the stress angle change exceeds 10 degrees. Note that the threshold of angle change may need a tune-up (up to 90 degrees) under a small horizontal stress contrast. Figure 10 shows the angle change of S_{Hmax} and impact radius in the producing layer. Within 5 years of parent-well production, the orientation change of S_{Hmax} is below 30 degrees. A white ellipse is drawn to outline the affected region where the angle change exceeds 10 degrees, and the impact radius is determined accordingly along its semi-minor axis. For Well H1-2, the impact radius in the producing layer keeps enlarging, and the estimated impact radius is 128 m and 192 m, respectively, at 2 and 5 years of parent-well production.

As shown in Fig. 11, the impact radius of stress reorientation is also evaluated in the upper potential pay zones. The impact radius increases rapidly in the first few years and tends to smooth down at the later production stage. Besides, the farther the vertical distance to the producing layer, the smaller the impact radius. Results show that for Well H1-2, the impact radius in the producing layer is up to 265 m but is limited to 145 m in

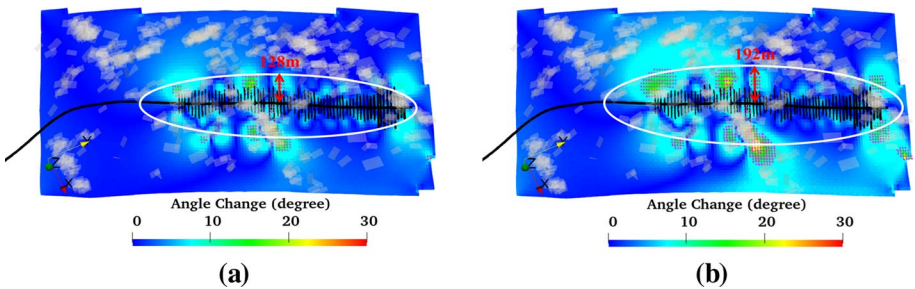
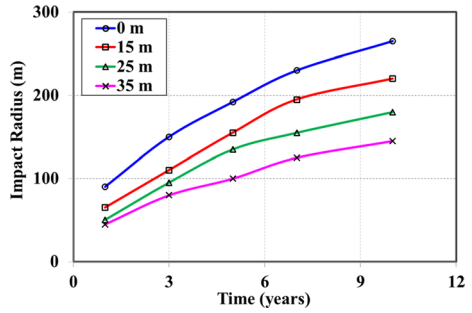


Fig. 10 Comparison of the angle change of S_{Hmax} in the producing layer at **a** 2 years and **b** 5 years of Well H1-2 production. The purple dots represent the location where the angle change exceeds 10 degrees, the white ellipses approximate the affected boundary, and the red arrows represent the impact radius

Fig. 11 Summary of the impact radius of stress reorientation in different pay zones along with production time. The legend refers to the vertical distance from a specific potential layer to the producing layer of Well H1-2



the top potential layer that is 35 m vertically away. These values can be used to estimate the minimum parent–child horizontal spacing to avoid undesirable fracture curving from infill wells. For example, the horizontal spacing between parent and child wells should be greater than 265 m in the producing layer of Well H1-2.

3.1.3 Parent–Child Well Spacing Optimization

The 3D stress analysis indicates that the depletion-induced stress redistribution and reorientation not only occur in the producing layer but spread toward the adjacent potential pay zones. Therefore, the child-well fractures may not propagate as desired if the parent and child wells are not spaced reasonably. Under the depletion-induced heterogeneous stress field, this section optimizes the parent–child horizontal and vertical spacing based on child-well fracturing results. To follow an emerging hydraulic fracturing design practice in the Sichuan Basin, we use the input parameters listed in Table 3 to simulate the multi-cluster child-well fracture propagation in one stage with six perforation clusters separated at 10 m each.

For child wells to be placed in the producing layer, three parent–child horizontal spacing (300, 350, and 400 m) are investigated at 2 and 5 years of parent-well production. The three horizontal spacing candidates are selected upon both stress analysis (i.e., impact radius) and empirical knowledge, and so will the vertical spacing candidates in the following. Figure 12 shows the simulated child-well fracture geometry at different parent–child horizontal spacing after 5 years. Under 300 m horizontal spacing, a large portion of the child-well fracture deviates toward parent-well fractures. In contrast, moving the child well farther away from the parent well by 100 m leads to relatively symmetric bi-wing fractures. As illustrated above, the fast pressure depletion around the parent well induces an obvious

Table 3 Hydraulic fracture model parameters for child-well fracturing

Parameter	Value	Unit
Number of clusters	6	–
Perforation cluster spacing	10	m
Pumping time	125	min
Pumping rate	16	m ³ /min
Slurry volume	2000	m ³
Proppant mass	206400	kg

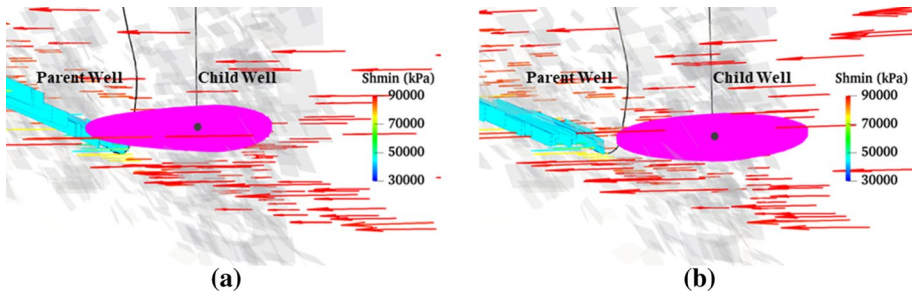


Fig. 12 Effect of stress changes on child-well fracture geometry at **a** 300 m horizontal spacing and **b** 400 m horizontal spacing after 5 years of Well H1-2 production. The cyan and magenta planes are parent-well fractures and child-well fractures, respectively. The orientation of S_{Hmax} and magnitude of S_{Hmin} are represented by the arrow directions and colors, respectively. One fracturing stage with six perforation clusters is modeled with one representative child-well fracture displayed for clear visualization

stress sink (i.e., small S_{Hmin}) over the SRV region, which consequently attracts child-well fractures and results in horizontal asymmetry.

A horizontal asymmetry factor (i.e., total length of fracture segments on the side close to the parent well over total length of all fracture clusters) is defined to quantify the length asymmetry of child-well fractures. Ideally, a horizontal asymmetry factor of 0.5 is desirable under the prior depletion effects as more intact rock can be stimulated by the newly created fractures. However, considering the actual geological complexity, we assume all horizontal asymmetry factors below 0.53 (roughly 5% offset to the ideal value) are acceptable. A summary of the horizontal asymmetry factors at different production stages is presented in Table 4. At 2 years of parent-well production, the horizontal asymmetric growth of child-well fractures is negligible at horizontal offset larger than 350 m. Hence, the optimal parent–child horizontal spacing can be chosen as 350 m to avoid asymmetric fracture propagation while guaranteeing relatively high well coverage and gas production. However, at 5 years, the 300 m and 350 m horizontal spacings lead to obvious child-well fracture deviation; thus, we recommend 400 m as the parent–child horizontal spacing.

For child wells to be placed in the upper potential layers, three parent–child vertical spacing (15, 25, and 35 m) are investigated at two horizontal offsets (175 and 200 m) after 2 and 5 years. As shown in Fig. 13b, at 35 m vertical spacing, the child-well fracture is vertically symmetric to the horizontal wellbore at 2 years. In comparison, Fig. 13a, d indicates that the child-well fracture tends to slightly propagate toward the parent-well fractures in the vertical direction when reducing parent–child vertical offset or elongating parent-well production. The vertical asymmetric growth becomes most significant in Fig. 13c, wherein the child well is infilled after 5 years and at 15 m vertical spacing. Similar to the horizontal

Table 4 Summary of horizontal asymmetry factor at different production stages of Well H1-2

Horizontal asymmetry factor	Parent–child horizontal spacing		
	300 m	350 m	400 m
At 2 years of parent-well production	0.55	0.51	0.50
At 5 years of parent-well production	0.60	0.55	0.52

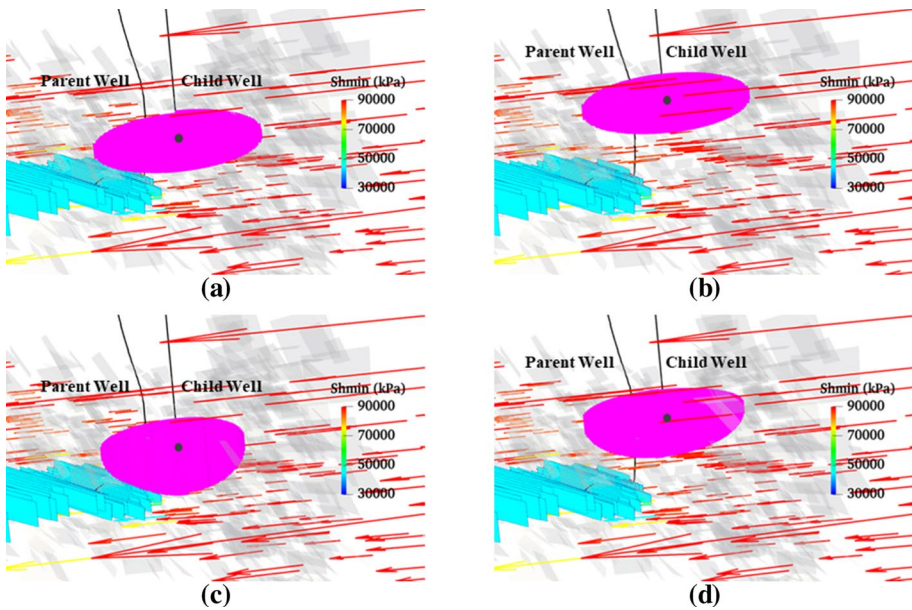


Fig. 13 Effect of Well H1-2-induced stress changes on child-well fracture geometry at **a** 15 m vertical spacing after 2 years, **b** 35 m vertical spacing after 2 years, **c** 15 m vertical spacing after 5 years, and **d** 35 m vertical spacing after 5 years. The parent–child horizontal offset is 175 m, and the cyan and magenta planes are parent-well fractures and child-well fractures, respectively. The orientation of S_{Hmax} and magnitude of S_{Hmin} are represented by the arrow directions and colors, respectively. One fracturing stage with six perforation clusters is modeled with one representative child-well fracture displayed for clear visualization

asymmetric growth, the vertical asymmetry of child-well fractures is also attributed to the depletion-induced stress sink over the SRV region.

To quantify the height asymmetry of child-well fractures, we define a vertical asymmetry factor (i.e., total height of fracture segments on the side close to the parent well over total height of all fracture clusters) to evaluate the spatial configuration of fracture height. Likewise, a vertical asymmetry factor of 0.53 is assumed as the threshold to differentiate between effective and ineffective fracture height propagation. Table 5 shows that a wide range of parent–child offset is acceptable if the infill well is drilled at 2 years in the upper potential target. However, to ensure a higher recovery efficiency, we suggest a relatively tight parent–child horizontal and vertical spacing of 175 m and 15 m, respectively. Guided by the same principle, the parent–child vertical spacing should be 35 m with a horizontal spacing of 175 m at the end of 5 years.

Table 5 Summary of vertical asymmetry factor at different production stages of Well H1-2

Vertical asymmetry factor	Parent–child vertical spacing @ 2 years			Parent–child vertical spacing @ 5 years		
	15 m	25 m	35 m	15 m	25 m	35 m
Horizontal spacing, 175 m	0.52	0.50	0.50	0.66	0.56	0.52
Horizontal spacing, 200 m	0.50	0.50	0.50	0.60	0.55	0.51

3.2 Type II: Clustered Natural Fracture Pattern

The clustered natural fracture pattern is identified around Well H10-4, and most clustered natural fractures tend to extend parallel to the horizontal wellbore. Within this sector model, there are 2706 natural fractures in total. The reservoir dimensions in the x -, y -, and z -direction are 2000, 3000, and 71.2 m, respectively, meshed into 100, 150, and 9 gridblocks. Vertically, Wufeng and Longmaxi 1^1 – 1^3 are each discretized into 1 row, and Longmaxi 1^4 is discretized into 5 rows. Well H10-4 has a lateral length of 2290 m and is drilled at an average landing depth of 3460 m to exploit the lower production target. To overcome the hindering effect of parallel, clustered natural fractures, the field operator has implemented a more intensive completion design on Well H10-4. Compared to Well H1-2, the main differences are doubling the proppant amount and shortening the perforation cluster spacing. The entire lateral section is fractured in 38 stages with 6–8 clusters per stage. Again, the integrated reservoir-geomechanics-fracture model is employed to calibrate the reservoir and fracture properties, investigate the depletion-induced stress changes, and optimize the parent–child well spacing upon the hydraulic fracture modeling.

3.2.1 History Matching

Well H10-4 has been produced since early 2021, so we only have 82 days of production data available for history matching. The reservoir model is calibrated under the constraint of gas rates, as shown in Fig. 14a, to match the BHPs and water rates by tuning reservoir and hydraulic/natural fracture properties. The history-matched fracture permeability decay coefficient is 0.05 MPa^{-1} , and the calibrated relative permeability curves are shown in Fig. 14b. A good agreement between simulated and history BHPs and water rates is shown in Fig. 14c, d, respectively. More detailed reservoir and fracture parameters of Well H10-4 can be found in Table 6.

3.2.2 Spatiotemporal Stress Evolution

In comparison, the target region where parallel, clustered natural fractures are widely distributed bears relatively high in situ stresses. The magnitude of S_{hmin} is 100 MPa, which is 10 MPa higher than that in the orthogonal natural fracture region, and the horizontal stress contrast ($S_{\text{Hmax}} - S_{\text{hmin}}$) is 15 MPa. Since Well H10-4 is still at the early stage of production, the logging and fracturing reports only provide by-layer data of Young's modulus and Poisson's ratio. As shown in Fig. 15, the average Young's modulus and Poisson's ratio over this area are 43 GPa and 0.24, respectively. Upon the 3D geomechanics model setup, we simulate the orientation change of S_{Hmax} and the magnitude change of S_{hmin} in the 10 years of Well H10-4 production.

Figure 16 shows the pore pressure and S_{hmin} distribution at different production stages. Similar to what we have observed in the orthogonal natural fracture case, the drainage volume of pore pressure and S_{hmin} enlarges as gas depletion continues. However, due to the poroelastic effect, the pressure drop contrarily causes an increase in the effective stresses. This type of counteraction makes the total principal stresses, such as S_{hmin} , decay much slower than the pore pressure, as shown in Fig. 16a, c or Fig. 16b, d. Besides, the drainage volume not only evolves around the horizontal wellbore but the large natural fracture clusters. The more complex pressure and stress changes increase the chances of fracture hits

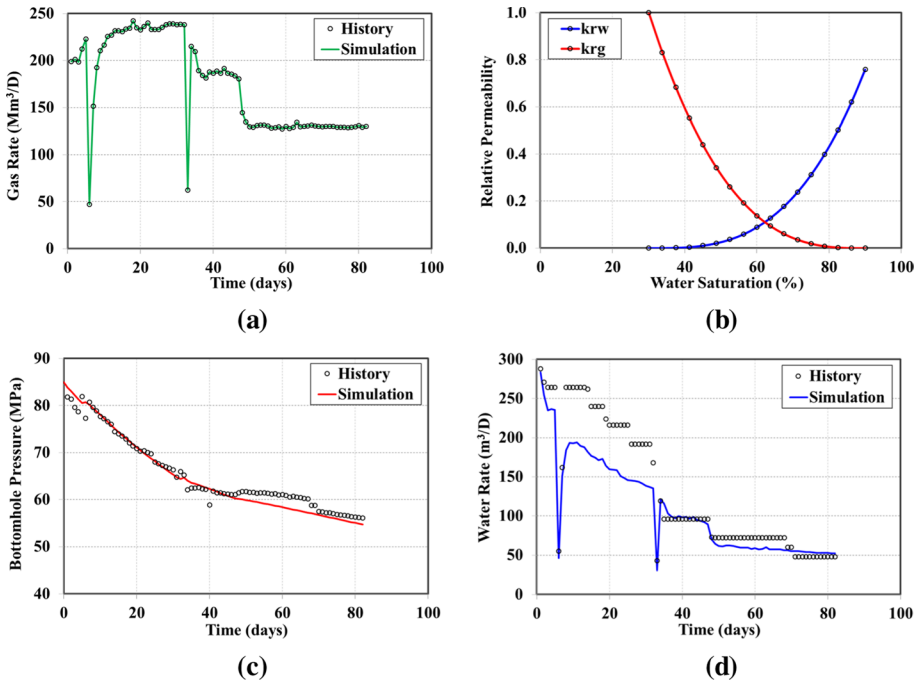


Fig. 14 History matching results for Well H10-4 with **a** gas rates as matching constraint, **b** history-matched relative permeability curves, **c** historical and simulated BHPs, and **d** historical and simulated water rates

Table 6 Calibrated reservoir and fracture parameters of Well H10-4

Reservoir properties	Value	Unit	Fracture properties	Value	Unit
Initial reservoir pressure	85	MPa	Horizontal lateral length	2290	m
Reservoir temperature	150	°C	Number of stages	38	–
Average reservoir porosity	4.9	%	Number of clusters	237	–
Horizontal permeability	59	nD	Perforation cluster spacing	9.62	m
Vertical permeability	0.6	nD	Average fracture half-length	53	m
Rock compressibility	4.35×10^{-4}	MPa^{-1}	Average fracture height	6.39	m
Matrix water saturation	30	%	Hydraulic fracture conductivity	56	mD-m
Irreducible gas saturation	10	%	Natural fracture conductivity	11	mD-m
Langmuir volume	0.004	m^3/kg	Fracture perm decay coeff	0.05	MPa^{-1}
Langmuir pressure	10.3	MPa	Fracture water saturation	78.7	%
Bulk density	2600	kg/m^3	Number of natural fractures	2706	–

or poor child-well performance, thus requiring more attention to the risk aversion of infill drilling. The statistical analysis of pore pressure and S_{hmin} distribution over the SRV region is shown in Fig. 17. At 2 years of parent-well production, the P50 of pore pressure drops from 85 to 80 MPa and S_{hmin} from 100 to 98 MPa, so the decrease in S_{hmin} is 40% of pore

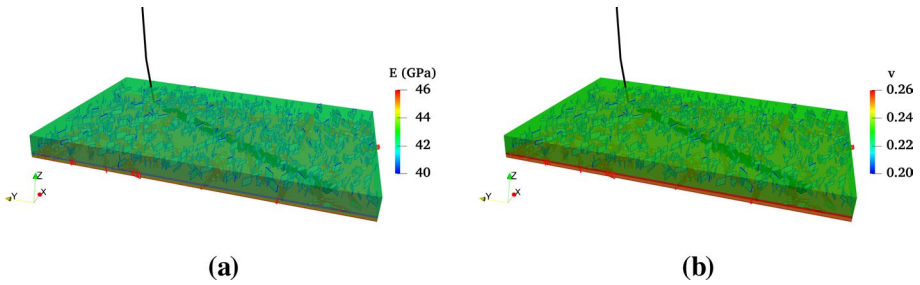


Fig. 15 By-layer distribution of **a** Young's modulus and **b** Poisson's ratio. The gray surfaces with red edges represent parallel, clustered natural fractures, the gray surfaces with blue edges represent orthogonal natural fractures, and the black line represents the trajectory of the horizontal wellbore

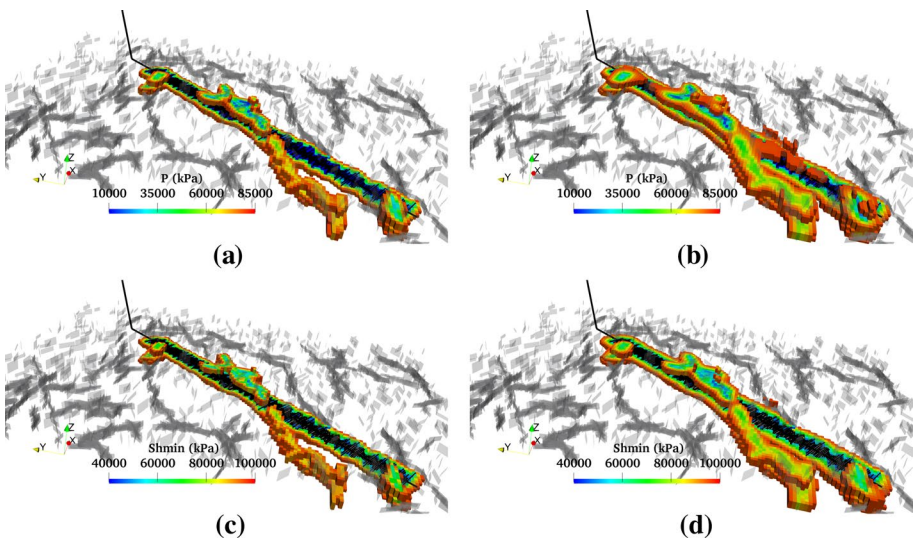


Fig. 16 Comparison of pore pressure and S_{hmin} changes around Well H10-4 with **a** pore pressure distribution at 2 years, **b** pore pressure distribution at 5 years, **c** S_{hmin} distribution at 2 years, and **d** S_{hmin} distribution at 5 years

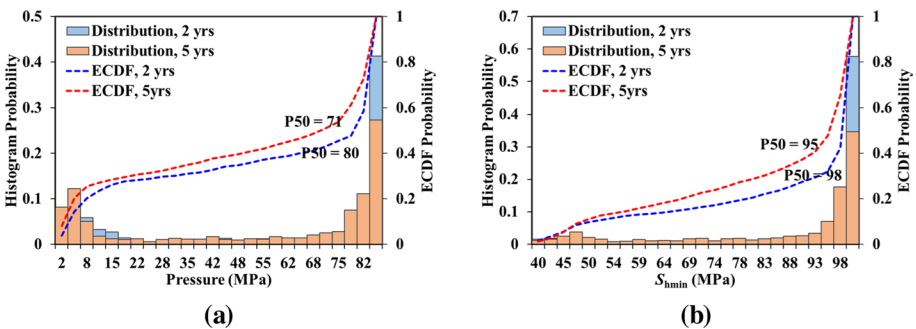


Fig. 17 Comparison of the histogram and ECDF probability between **a** pore pressure and **b** S_{hmin} over the SRV region at 2 and 5 years of Well H10-4 production

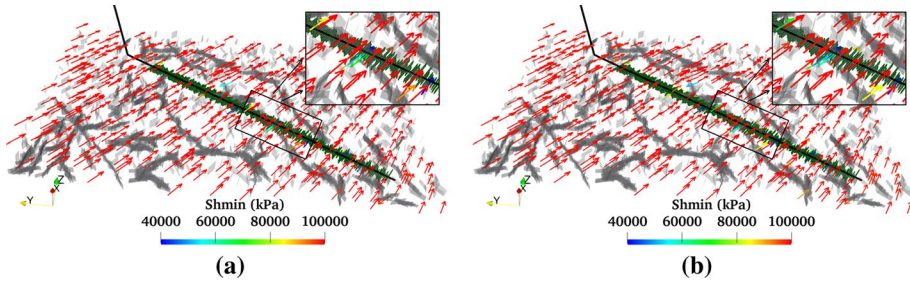


Fig. 18 Comparison of the orientation of S_{Hmax} (arrow directions) and magnitude of S_{hmin} (arrow colors) at **a** 2 years and **b** 5 years of Well H10-4 production

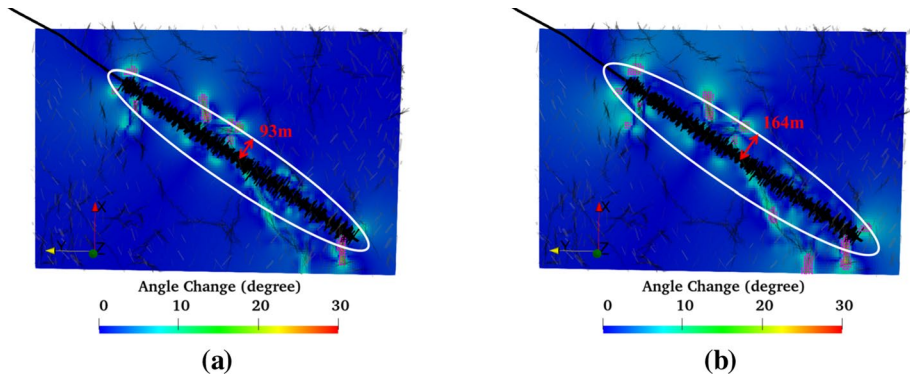
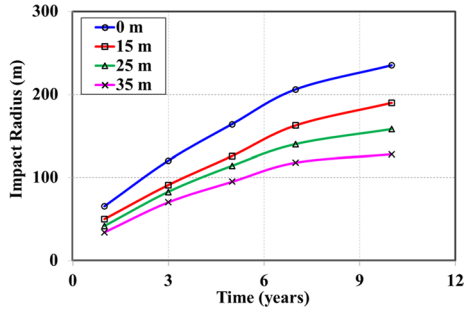


Fig. 19 Comparison of the angle change of S_{Hmax} in the producing layer at **a** 2 years and **b** 5 years of Well H10-4 production. The purple dots represent the location where the angle change exceeds 10 degrees, the white ellipses approximate the affected boundary, and the red arrows represent the impact radius

pressure change. This relative ratio drops to around 36% at 5 years as the pore pressure change becomes much steadier at later stages.

Though the magnitude change of S_{hmin} is obvious, the S_{Hmax} reorientation is negligible since the horizontal stress contrast in this case (15 MPa) is even higher than that in the orthogonal natural fracture case. As shown in Fig. 18, most arrows keep pointing perpendicular to the horizontal wellbore after 5 years of parent-well production. The stress difference between 2 and 5 years lies in the magnitude of S_{hmin} , as indicated by the arrow colors near the wellbore, instead of the orientation of S_{Hmax} . Still, we quantify the angle change of S_{Hmax} following the definition of impact radius defined above. In the producing layer of Well H10-4, as in Fig. 19, the S_{Hmax} reorientation is below 30 degrees for the first 5 years. The impact radius is estimated as 93 m and 164 m, respectively, at the end of 2 and 5 years, which are approximately 75% to these of the orthogonal natural fracture case. As observed in the field practice, the parallel, clustered natural fractures in Sichuan Basin impede the extension of hydraulic fractures, thus shrinking the affected area of stress reorientation. To be noted, though the orientation change of S_{Hmax} is not as significant as in the orthogonal case, the pressure drainage through clustered natural fractures may induce localized stress sink and increase the chance of fracture hits if the child well is not placed properly.

Fig. 20 Summary of the impact radius of stress reorientation in different pay zones along with production time. The legend refers to the vertical distance from a specific potential layer to the producing layer of Well H10-4



Based on the 3D stress modeling, we also summarize the impact radius of stress reorientation in the upper potential layers. As shown in Fig. 20, the producing layer still preserves the largest impact radius, and the top potential layer bears the least influence. The maximum impact radius in the producing layer is 235 m at the end of 10 years and 128 m in the top potential layer. Therefore, if an infill well is drilled in the top potential layer, a potential horizontal spacing between Well H10-4 and the child well should be greater than 128 m to avoid possible fracture curving.

3.2.3 Parent–Child Well Spacing Optimization

Clustered natural fractures induce strong complexity in the local stress redistribution. As shown in Fig. 16, an irregular stress sink is created along with the large natural fracture cluster near the lateral toe. It would be quite challenging to place an infill well close to those clustered natural fractures as the localized stress sink may attract child-well fractures and cause interwell interference. Or on the other hand, the parallel, clustered natural fractures may inhibit the extension of child-well fractures in highly stressed formations. To uncover the underlying mechanism, we investigate the child-well fracture propagation near the localized stress sink induced by clustered natural fractures. The same fracturing parameters in Table 3 are used, and the parent–child horizontal and vertical offsets are optimized accordingly.

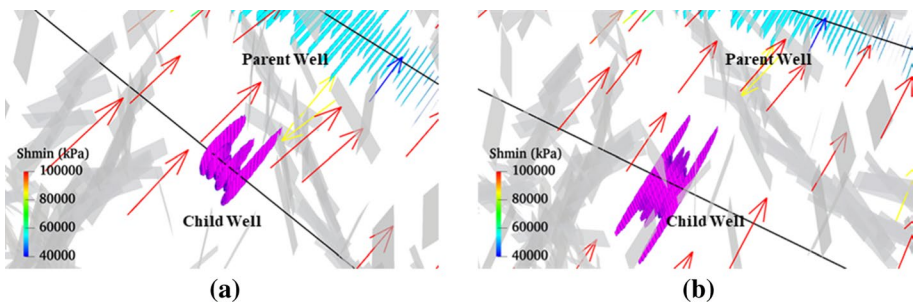


Fig. 21 Effect of stress changes on child-well fracture geometry at **a** 300 m horizontal spacing and **b** 400 m horizontal spacing after 5 years of Well H10-4 production. The cyan and magenta planes are parent-well fractures and child-well fractures, respectively. The orientation of S_{Hmax} and magnitude of S_{Hmin} are represented by the arrow directions and colors, respectively. One fracturing stage with six perforation clusters is modeled

Three parent–child horizontal spacing (300, 350, and 400 m) are modeled for infill-well placement in the producing layer at 2 and 5 years of parent-well production. Figure 21 compares the child-well fracture geometry for infill wells drilled at different horizontal offsets. Again, an obvious asymmetric growth is observed when the child well is 300 m away from the parent well. On the other hand, the child-well fractures initiated 400 m away present more extended length and symmetric geometry even at the end of 5 years. These differences are attributed to the coefficients of two critical factors—under the dense well layout, the child well is closer to the localized stress sink associated with clustered natural fractures, which significantly attracts the child-well fractures and leads to asymmetry growth of fracture length; the clustered natural fractures in-between parent and child wells (i.e., gray surfaces between parent and child wells in Fig. 21) are almost perpendicular to the orientation of S_{Hmax} , hence resulting in negative net pressure when child-well fractures are about to divert into natural fractures and preventing child-well fractures from further propagation.

Since the child well is placed near the cluster-induced localized stress sink, the horizontal asymmetry factor tends to be higher than that under the orthogonal natural fracture pattern. Table 7 summarizes the horizontal asymmetry factor of child-well fractures at different production stages. At 2 years of parent-well production, a horizontal offset greater than 350 m would guarantee the horizontal asymmetry factor smaller than 0.53. However, when infill drilling occurs at 5 years, the length asymmetry of child-well fractures becomes more significant, with all horizontal asymmetry factors larger than or equal to 0.53. Hence, we recommend the child well in the same layer be drilled 400 m away from the parent well at 2 or 5 years.

For stacked and staggered infill-well layouts, we investigate three parent–child vertical spacing (15, 25, and 35 m) at two horizontal offsets (175 and 200 m) after 2 and 5 years. Figure 22 shows a similar trend in fracture height asymmetry as the orthogonal natural fracture pattern; that is, the vertical asymmetric growth of child-well fractures becomes more significant as production time increases or vertical spacing decreases. In addition, a comparison of Figs. 13 and 22 indicates that child-well fracture length in the latter tends to deviate more toward the parent-well fractures. This is consistent with what we have discussed above—the localized stress sink induced by large natural fracture clusters would significantly attract child-well fractures and aggravate fracture length asymmetry. Thus, both the horizontal and vertical spacing should be carefully evaluated for child wells to be placed in the clustered natural fractures region to ensure the effective growth of child-well fracture length and height.

Table 8 presents a summary of the vertical asymmetry factor for child-well fractures. At 2 years of parent-well production, all tested cases give a vertical asymmetry factor of around 0.50, which means the depletion-induced stress decrease is not strong enough to trigger asymmetric fracture height growth. The optimal parent–child horizontal and vertical spacings are recommended as 175 m and 15 m, respectively, to guarantee the well density and high recovery efficiency. However, another 3 years of production significantly

Table 7 Summary of horizontal asymmetry factor at different production stages of Well H10-4

Horizontal asymmetry factor	Parent–child horizontal spacing		
	300 m	350 m	400 m
At 2 years of parent-well production	0.58	0.54	0.51
At 5 years of parent-well production	0.65	0.57	0.53

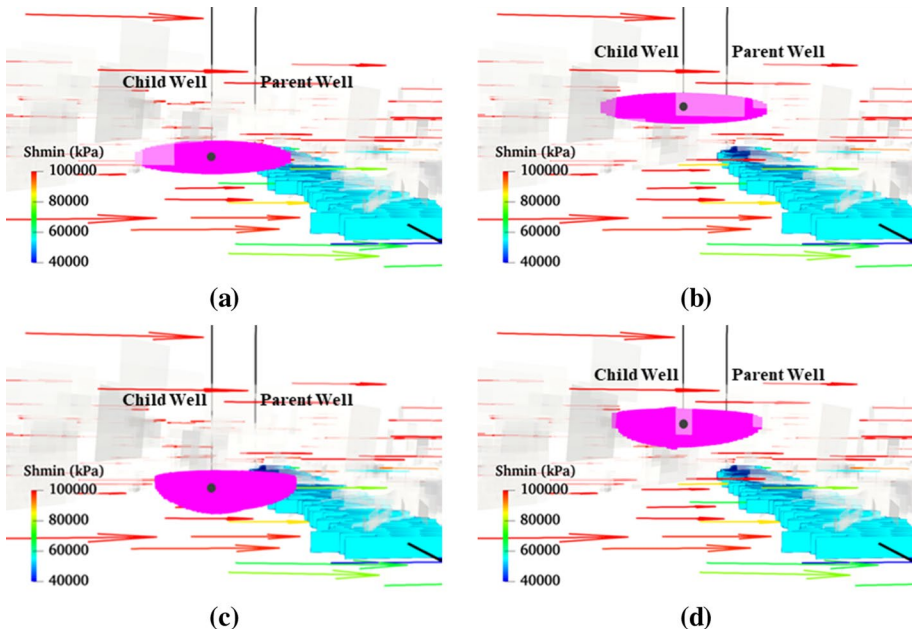


Fig. 22 Effect of Well H10-4-induced stress changes on child-well fracture geometry at **a** 15 m vertical spacing after 2 years, **b** 35 m vertical spacing after 2 years, **c** 15 m vertical spacing after 5 years, and **d** 35 m vertical spacing after 5 years. The parent–child horizontal offset is 175 m, and the cyan and magenta planes are parent-well fractures and child-well fractures, respectively. The orientation of S_{Hmax} and magnitude of S_{Hmin} are represented by the arrow directions and colors, respectively. One fracturing stage with six perforation clusters is modeled with one representative child-well fracture displayed for clear visualization

Table 8 Summary of vertical asymmetry factor at different production stages of Well H10-4

Vertical asymmetry factor	Parent–child vertical spacing @ 2 years			Parent–child vertical spacing @ 5 years		
	15 m	25 m	35 m	15 m	25 m	35 m
Horizontal Spacing, 175 m	0.51	0.50	0.50	0.62	0.55	0.52
Horizontal Spacing, 200 m	0.50	0.50	0.50	0.56	0.52	0.50

increases the extent of fracture height asymmetry, and there are only three locations that preserve a relatively symmetric fracture height growth (vertical asymmetry factor smaller than 0.53). Considering the possible fracture length deviation at a smaller horizontal offset, we suggest the child well be drilled 25 m vertically away from the parent well with a horizontal spacing of 200 m.

3.3 Discussion

3.3.1 Comparison Between Types I and II

Two representative wells, Well H1-2 and Well H10-4, are modeled to illustrate the impact of complex natural fracture settings on parent–child well spacing. Well H1-2 is drilled in the region with orthogonal natural fractures and Well H10-4 in the region with parallel, clustered natural fractures. Based on the multiphysics integrated reservoir-geomechanics-fracture modeling, we have summarized the following three main differences between orthogonal (Type I) and clustered (Type II) natural fracture patterns:

1. Parent-well fracture volume. The history-matched hydraulic fracture half-length, height, and conductivity in the orthogonal fracture case are 73 m, 6.82 m, and 130 mD-m, respectively, much larger than those in the clustered natural fracture case that are 53 m, 6.39 m, and 56 mD-m. Regarding the hindering effects of clustered natural fractures that are parallel to the horizontal wellbore, an intensive completion design is suggested on-site to improve the hydraulic fracturing effect.
2. Spatiotemporal stress evolution. Though parallel, clustered natural fractures constrain the propagation of hydraulic fractures, some may behave as additional flow channels if they interact with hydraulic fractures. Hence, the pore pressure and stress distribution in Type II tend to be more irregular than in the orthogonal natural fracture case. Placing an infill well in reservoirs with clustered natural fractures should be cautious, and a larger parent–child horizontal spacing may be required to avoid possible fracture hits and interwell interference.
3. Child-well fracture asymmetry. The production-disturbed stress state affects both the length and height asymmetry of child-well fractures. Figure 23a compares the horizontal asymmetry factor between two natural fracture patterns for child wells drilled in the producing layer. It shows that Type II is more prone to trigger fracture length deviation since the child well is placed near the cluster-induced localized stress sink. Meanwhile, Fig. 23b shows that Type I induces more significant fracture height asymmetry when infill wells are staggered in the upper potential layers, mainly due to its greater parent-well fracturing volume.

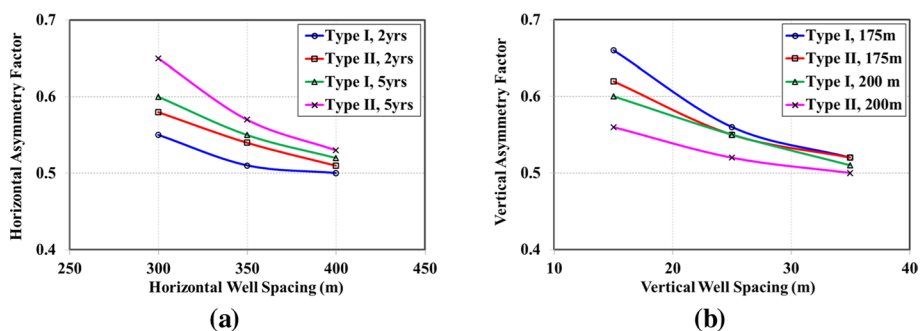


Fig. 23 Comparison between Types I and II for **a** horizontal asymmetry factor at 2 and 5 years of parent-well production and **b** vertical asymmetry factor at 175 and 200 m horizontal offsets. The left is evaluated for child wells drilled in the producing layer, and the right is for child wells fractured at the end of 5 years

Table 9 Summary of optimal parent–child well spacing for two complex natural fracture patterns

Parent–child well spacing (horizontal + vertical)	Type I—orthogonal natural fractures	Type II—clustered natural fractures
At 2 years of parent-well production	175 m + 15 m	175 m + 15 m
At 5 years of parent-well production	175 m + 35 m	200 m + 25 m

As placing parent and child wells in different pay zones becomes a thriving option, we restate the stacked/staggered parent–child well spacing at different infill timings in Table 9. Because the depletion-induced stress changes at 2 years are still moderate, the most compact parent–child well placement (horizontal spacing of 175 m + vertical spacing of 15 m) works for both natural fracture patterns. At 5 years of parent-well production, a horizontal spacing of 175 m still applies to Type I but should be enlarged in Type II (200 m) considering the interaction between hydraulic and clustered natural fractures. Moreover, the greater parent-well fracture volume in Type I requires a larger vertical spacing (35 m) to avoid significant fracture height asymmetry, whereas a vertical spacing of 25 m is applicable in Type II.

3.3.2 Limitation of This Study

The enhanced integrated reservoir-geomechanics-fracture model incorporates the geomechanics effects in well spacing optimization, captures the spatiotemporal stress evolution under complex natural fractures, and provides rules of thumb for infill-well placement. However, there still exist several limits at the current stage: (1) only gas desorption but Knudsen diffusion and gas slippage is considered for the fluid-flow modeling of shale gas, and the geomechanics model is derived based on an isothermal linear elastic assumption; (2) the matrix or fracture permeability is updated as a function of pressure drawdown, which may not be accurate enough to reflect the flow and mechanics interaction and iteratively or fully coupling should be incorporated in future work to better demonstrate the matrix/fracture property changes; (3) the co-simulation of parent-well and child-well production is not performed in this work, and the parent–child well spacing is optimized based on the child-well fracturing effectiveness; (4) this study focuses on the stress evolution and child-well placement near a single parent well and does not consider the symmetric parent–child well layout (e.g., one child well in-between two parent wells).

4 Conclusions

Based on a multiphysics, integrated reservoir-geomechanics-fracture model, this work comprehensively simulated the 3D spatiotemporal stress evolution in a deep shale gas reservoir of the Sichuan Basin, Western China, and quantitatively determined the optimal parent–child well spacing at different infill timings. Two complex natural fracture patterns (i.e., orthogonal and clustered natural fractures) were identified around Well H1-2 and Well H10-4, respectively, so these two wells were modeled to demonstrate their geomechanics responses under different natural fracture settings. For each case, history matching was first performed to calibrate the reservoir and hydraulic/natural fracture properties. The 3D pressure and stress evolution were then simulated using the EDFM-FEM-based fluid flow

and geomechanics coupling model. Finally, with an updated heterogeneous stress state, the DDM hydraulic fracture model was applied to simulate the simultaneous propagation of multicluster child-well fractures. The effects of stress redistribution on child-well fracture geometry were examined under different horizontal and vertical offsets, and the optimal parent–child well spacing was recommended for infill drilling either in the same or adjacent layers. The field case studies showed the following:

1. The deep shale gas reservoir in the Sichuan Basin is highly stressed, with minimum horizontal stress of 90–100 MPa and horizontal stress contrast of 12–15 MPa; hence, the orientation change of S_{Hmax} is minor (below 30 degrees), and the resultant child-well fracture curving is not obvious.
2. Due to the fast pore pressure depletion, the magnitude of S_{hmin} drops within the SRV region in the producing layer and the SRV projection region in the adjacent potential layers. In detail, the decrease in S_{hmin} is 30–50% of pore pressure change within 5 years of parent-well production. The production-associated localized stress sink increases the risks of fracture hits and interwell interference.
3. For infill wells to be drilled in the same layer as the parent well, decreasing the parent–child horizontal offset or elongating the production time both aggravates the asymmetry extent of child-well fracture length. A greater parent–child well spacing is required when the child well is placed near the cluster-induced localized stress sink to avoid significant length deviation of child-well fractures.
4. Placing infill wells in adjacent potential layers requires special attention to the height extension of child-well fractures. Under the current depletion rate, child-well fractures do not vertically deviate toward the parent well at the early stage of parent-well production. However, infill drilling upon large parent-well fracturing volume or after a long period of parent-well production should be distantly spaced to the parent well.
5. In the target deep shale gas reservoir, the parent–child horizontal spacing for infill drilling in the same layer is 350–400 m. For stacked and staggered infill-well layouts, the parent–child horizontal and vertical spacing are suggested as 175 m and 15 m, respectively, at 2 years of parent-well production. At the end of 5 years, we recommend a horizontal spacing of 175 m and vertical spacing of 35 m for the orthogonal natural fracture pattern, and 200 m and 25 m, respectively, for the clustered natural fracture pattern.

Acknowledgements This research was supported by the Reservoir Simulation Joint Industry Project at the Center for Subsurface Energy and the Environment at the University of Texas and SimTech LLC. We acknowledge Petrochina Southwest Oil & Gas Field Company for authorizing the publication of this work.

Declarations

Conflict of interest The authors declare that they have no conflict of interest.

References

Ajisafe, F.O., Solovyeva, I., Morales, A., Ejofodomi, E., Marongiu-Porcu, M.: Impact of well spacing and interference on production performance in unconventional reservoirs, Permian Basin. Presented

- at the SPE/AAPG/SEG Unconventional Resources Technology Conference, Austin, Texas, USA, 24–26 July. URTEC-2690466-MS (2017). <https://doi.org/10.15530/URTEC-2017-2690466>
- Bachman, R.C., Sen, V., Khalmanova, D., M'Angha, V.O., Settari, A.: Examining the effects of stress dependent reservoir permeability on stimulated horizontal montney gas wells. Presented at the Canadian Unconventional Resources Conference, Calgary, Alberta, Canada, 15–17 November. SPE-149331-MS (2011). <https://doi.org/10.2118/149331-MS>
- Behm, E., Al Asimi, M., Al Maskari, S., Juna, W., Klie, H., Le, D., Lutidze, G., Rastegar, R., Reynolds, A., Tathed, V., Younis, R., Zhang, Y.: Middle east steamflood field optimization demonstration project. Presented at the Abu Dhabi International Petroleum Exhibition & Conference, Abu Dhabi, UAE, 11–14 November. SPE-197751-MS (2019). <https://doi.org/10.2118/197751-MS>
- Biot, M.A.: General theory of three-dimensional consolidation. *J. Appl. Phys.* **12**(2), 155–164 (1941). <https://doi.org/10.1063/1.1712886>
- Biot, M.A.: Theory of elasticity and consolidation for a porous anisotropic solid. *J. Appl. Phys.* **26**(2), 182–185 (1955). <https://doi.org/10.1063/1.1721956>
- Chen, J., Wei, Y., Wang, J., Yu, W., Qi, Y., Wu, J., Luo, W.: Inter-well interference and well spacing optimization for shale gas reservoirs. *J. Nat. Gas Geosci.* **6**(5), 301–312 (2021). <https://doi.org/10.1016/j.jnggs.2021.09.001>
- Defeu, C., Williams, R., Shan, D., Martin, J., Cannon, D., Clifton, K., Lollar, C.: Case study of a landing location optimization within a depleted stacked reservoir in the Midland Basin. Presented at the SPE Hydraulic Fracturing Technology Conference and Exhibition, The Woodlands, Texas, USA, 5–7 February. SPE-194353-MS (2019). <https://doi.org/10.2118/194353-MS>
- Guo, X., Wu, K., Killough, J.: Investigation of production-induced stress changes for infill-well stimulation in Eagle Ford Shale. *SPE J.* **23**(04), 1372–1388 (2018). <https://doi.org/10.2118/189974-PA>
- Jun, Q., Xian, C., Liang, X., Zhao, C., Wang, G., Wang, L.: Characterizing and modeling multi-scale natural fractures in the Ordovician-Silurian Wufeng-Longmaxi Shale Formation in South Sichuan Basin. Presented at the SPE/AAPG/SEG Unconventional Resources Technology Conference, Austin, Texas, USA, 24–26 July. URTEC-2691208-MS (2017). <https://doi.org/10.15530/URTEC-2017-2691208>
- Langmuir, I.: The adsorption of gases on plane surfaces of glass, mica and platinum. *J. Am. Chem. Soc.* **40**(9), 1361–1403 (1918). <https://doi.org/10.1021/ja02242a004>
- Li, L., Lee, S.H.: Efficient field-scale simulation of black oil in a naturally fractured reservoir through discrete fracture networks and homogenized media. *SPE Reserv. Eval. Eng.* **11**(04), 750–758 (2008). <https://doi.org/10.2118/103901-PA>
- Li, T., Razavi, O., Olson, J.E.: Modeling fracture in layered formations using a simplified 3D displacement discontinuity method. Paper presented at the 52nd U.S. Rock Mechanics/Geomechanics Symposium, Seattle, Washington, USA, 17–20 June. ARMA-2018-1079 (2018)
- Liang, X., Liu, X., Shu, H., Xian, C., Zhang, Z., Zhao, C., Li, Q., Zhang, L.: Characterization of complex multiscale natural fracture systems of the Silurian LongMaXi Gas Shale in the Sichuan Basin, China. Presented at the SPE Asia Pacific Unconventional Resources Conference and Exhibition, Brisbane, Australia, 9–11 November. SPE-176938-MS (2015). <https://doi.org/10.2118/176938-MS>
- Lindsay, G., Miller, G., Xu, T., Shan, D., Baihly, J.: Production performance of infill horizontal wells vs. pre-existing wells in the major US unconventional basins. Presented at SPE Hydraulic Fracturing Technology Conference and Exhibition, The Woodlands, Texas, USA, 23–25 January. SPE-189875-MS (2018). <https://doi.org/10.2118/189875-MS>
- Liu, H.: *Fluid Flow in the Subsurface: History, Generalization and Applications of Physical Laws*. Springer, Cham (2017)
- Liu, L., Liu, Y., Yao, J., Huang, Z.: Efficient coupled multiphase-flow and geomechanics modeling of well performance and stress evolution in shale-gas reservoirs considering dynamic fracture properties. *SPE J.* **25**(03), 1523–1542 (2020). <https://doi.org/10.2118/200496-PA>
- Liu, Y., Kalinin, D., Li, D., Jiao, Y., Li, R.: Understanding the complexity of fracturing in the Sichuan Shale Gas Reservoir in China. Presented at the SPE/AAPG/SEG Asia Pacific Unconventional Resources Technology Conference, Brisbane, Australia, 18–19 November. URTEC-198248-MS (2019). <https://doi.org/10.15530/AP-URTEC-2019-198248>
- Marongiu-Porcu, M., Lee, D., Shan, D., Morales, A.: Advanced modeling of interwell-fracturing interference: an Eagle Ford shale-oil study. *SPE J.* **21**(05), 1567–1582 (2016). <https://doi.org/10.2118/174902-PA>
- Mi, L., Jiang, H., Mou, S., Li, J., Pei, Y., Liu, C.: Numerical simulation study of shale gas reservoir with stress-dependent fracture conductivity using multiscale discrete fracture network model. *Part. Sci. Technol.* **36**(2), 202–211 (2018). <https://doi.org/10.1080/02726351.2016.1241844>

- Moinfar, A., Varavei, A., Sepehrnoori, K., et al.: Development of an efficient embedded discrete fracture model for 3D compositional reservoir simulation in fractured reservoirs. *SPE J.* **19**(02), 289–303 (2014). <https://doi.org/10.2118/154246-PA>
- Olson, J.E.: Fracture aperture, length and pattern geometry development under biaxial loading: a numerical study with applications to natural, cross-jointed systems. *Spec. Publ.* **289**(1), 123–142 (2007). <https://doi.org/10.1144/SP289.8>
- Pei, Y., Yu, W., Sepehrnoori, K., Gong, Y., Xie, H., Wu, K.: The influence of development target depletion on stress evolution and infill drilling of upside target in the Permian Basin. *SPE Reserv. Eval. Eng.* **24**(03), 570–589 (2021). <https://doi.org/10.2118/205476-PA>
- Pei, Y., Yu, W., Sepehrnoori, K.: Investigation of vertical fracture complexity induced stress interference in multilayer shale gas reservoirs with complex natural fractures. Presented at the SPE Annual Technical Conference and Exhibition, Virtual, 26–29 October. SPE-201563-MS (2020). <https://doi.org/10.2118/201563-MS>
- Pei, Y., Sepehrnoori, K.: Investigation of parent-well production induced stress interference in multilayer unconventional reservoirs. *Rock Mech. Rock Eng.* **55**, 2965–2986 (2022). <https://doi.org/10.1007/s00603-021-02719-1>
- Roussel, N.P., Florez, H.A., Rodriguez, A.A.: Hydraulic fracture propagation from infill horizontal wells. Presented at SPE Annual Technical Conference and Exhibition, New Orleans, Louisiana, USA, 30 September–2 October. SPE-166503-MS (2013). <https://doi.org/10.2118/166503-MS>
- Safari, R., Lewis, R., Ma, X., Mutlu, U., Ghassemi, A.: Infill-well fracturing optimization in tightly spaced horizontal wells. *SPE J.* **22**(02), 582–595 (2017). <https://doi.org/10.2118/178513-PA>
- Sangnimmuan, A., Li, J., Wu, K.: Development of efficiently coupled fluid-flow/geomechanics model to predict stress evolution in unconventional reservoirs with complex-fracture geometry. *SPE J.* **23**(03), 640–660 (2018). <https://doi.org/10.2118/189452-PA>
- Sangnimmuan, A., Li, J., Wu, K., Holditch, S.: Impact of parent well depletion on stress changes and infill well completion in multiple layers in Permian Basin. Presented at SPE/AAPG/SEG Unconventional Resources Technology Conference, Denver, Colorado, USA, 22–24 July. URTEC-2019-972-MS (2019). <https://doi.org/10.15530/urtec-2019-972>
- Sepehrnoori, K., Xu, Y., Yu, W.: *Embedded Discrete Fracture Modeling and Application in Reservoir Simulation*. Elsevier: Developments in Petroleum Science, New York (2020)
- Settari, A.T., Bachman, R.C., Walters, D.A.: How to approximate effects of geomechanics in conventional reservoir simulation. Presented at the SPE Annual Technical Conference and Exhibition, Dallas, Texas, USA, 9–12 October. SPE-97155-MS (2005). <https://doi.org/10.2118/97155-MS>
- Wang, B., Fidelibus, C.: An open-source code for fluid flow simulations in unconventional fractured reservoirs. *Geosciences* **11**(2), 106 (2021). <https://doi.org/10.3390/geosciences11020106>
- Wang, T., Tian, S., Liu, Q., Li, G., Sheng, M., Ren, W., Zhang, P.: Pore structure characterization and its effect on methane adsorption in shale kerogen. *Pet. Sci.* **18**, 565–578 (2021). <https://doi.org/10.1007/s12182-020-00528-9>
- Wang, J., Lee, H.P., Li, T., Olson, J.E.: Three-dimensional analysis of hydraulic fracture effective contact area in layered formations with natural fracture network. Presented at the 54th U.S. Rock Mechanics/ Geomechanics Symposium, Virtual, 28 June–1 July. ARMA-2020-1967 (2020)
- Wu, K., Olson, J.E.: Simultaneous multifracture treatments: fully coupled fluid flow and fracture mechanics for horizontal wells. *SPE J.* **20**(02), 337–346 (2015). <https://doi.org/10.2118/167626-PA>
- Wu, K., Olson, J.E.: Numerical investigation of complex hydraulic-fracture development in naturally fractured reservoirs. *SPE Prod. Oper.* **31**(04), 300–309 (2016). <https://doi.org/10.2118/173326-PA>
- Xu, Y., Yu, W., Sepehrnoori, K.: Modeling dynamic behaviors of complex fractures in conventional reservoir simulators. *SPE Reserv. Eval. Eng.* **22**(03), 1110–1130 (2019). <https://doi.org/10.2118/194498-PA>
- Yu, W., Sepehrnoori, K.: Simulation of gas desorption and geomechanics effects for unconventional gas reservoirs. *Fuel* **116**, 455–464 (2014). <https://doi.org/10.1016/j.fuel.2013.08.032>

Publisher's Note Springer Nature remains neutral with regard to jurisdictional claims in published maps and institutional affiliations.